3D Printed Waveguide Filters: Manufacturing Process and Surface Mounted Assembly

Vicente Nova, Carmen Bachiller, Jordi Pascual-Folch, Álvaro Ferrer, Luis N. Ponce-Gonzalez, M. Luisa Marin and Vicente E. Boria, *Fellow, IEEE,*

***Abstract*—This paper presents a new approach to manufacturing and assembling inexpensive, lightweight devices using 3D-printed waveguides and surface-mount technology (SMT). Specifically, we have employed stereolithography (SLA) and a combination of electroless and electroplating processes to develop cavity filters in the X and C bands. The filters can be efficiently integrated into planar circuits via a reliable and simple transition that enables surface-mount assembly. Two resonator topologies, circular and rectangular, were examined and compared to develop X-band filters, and a triplet topology has been developed for the C-band. The measured frequency responses were consistent with simulations, with insertion losses below 2 and 1.43 dB for X and C bands, respectively. We have conducted several Monte Carlo analyses and a dimensional study to assess the impact of manufacturing tolerances on filter performance. Furthermore, a rectangular cavity resonator has been used to approximate the effective conductivity of the deposited copper coating, considering the detrimental effects of oxidation and surface roughness. The resulting effective conductivity of 17.7 MS/m was found to be higher than the current state-of-the-art values. Finally, SMT assembly offers several advantages over traditional methods, including reduced size, simplified assembly and integration with planar systems. The results presented in this work indicate that combining 3D printing and SMT provides a simple and efficient solution for developing lightweight and highly integrated components with superior performance.**

***Index Terms*—Additive manufacturing, bandpass filter, C band, monte carlo, substrate integration, surface-mount technology (SMT), tolerance analysis, X band, 3D printing.**

I. Introduction

THE next generation of satellite systems will consist of low-Earth orbit satellite mega-constellations or high-throughput geostationary satellites. This creates an urgent demand for communication filters with high-performance [1], [2]. Moreover, given the vast number of satellites required for mega-constellations, the long-term profitability of these new space systems necessarily depends on reducing manufacturing and launching costs [3], [4]. Therefore, integration, high-volume production, low mass, and size reduction have become critical considerations for developing new space communication components.

Despite the trend towards miniaturisation in the communication industry, metal-pipe waveguides and coaxial cables are still widely used in the space sector, due to their low loss and high power handling capability. However, these components are expensive, heavy, bulky, and unsuitable for mass production. Furthermore, these structures require complex assemblies to be connected with planar circuits, which presents a challenge for their interconnection with active devices [5]. These factors lead to a final system that is costly, bulky, and weighty, hindering its use in new satellite systems.

Over the last few decades, integrating waveguide and coaxial structures into planar substrates has presented a significant technological challenge of great practical relevance. Substrate Integrated Circuits (SICs) have emerged as a promising solution to implement non-planar structures into single or multi-layer substrates. This approach provides the advantage of using standard PCB manufacturing techniques and enabling easy integration with planar transmission lines, making it highly suitable for mass production [6]. However, the layered nature of these circuits limits the design flexibility and, therefore, the component performance. Furthermore, transitions between planar lines and SICs can be large and complex to design, sometimes requiring non-standard manufacturing processes. These limitations make SICs less suitable for the next generation of satellite systems, where high performance and design flexibility are crucial.

Surface-mount technology (SMT) has emerged as a promising approach for reducing costs and simplifying planar integration [7], [8]. The combination of advanced filter topologies, such as dielectric or cavity filters, and the SMT assembly provides an opportunity to develop high-performance filters with easy and affordable integration with planar circuits. Hybridising planar and non-planar structures is particularly advantageous for mass production, and can significantly reduce design and assembling costs. Despite several attempts to integrate cavities into an SMT form [7]–[10], the proposed approaches have been limited by high-precision manufacturing techniques or complex SMT transitions that hinder the filter performance, resulting in heavy or expensive components.

This article discusses the application of 3D printing to develop cavity filters with a simple surface-mounted assem-

Manuscript received 27 February 2023; revised XX February 2023; accepted XX February 2023. Date of publication XX February 2023; date of current version XX February 2023. This work was supported by the Agencia Valenciana de de la Innovación research project INNVA1/2020/84, by the Agencia Estatal de Investigación (Spain) under the Fellowship for Training PhDs BES-2017-079728, and by the Ministerio de Ciencia e Innovación (MICIN, Spanish Government) through the Research and Development project PID2019-103982RB-C41 (under grant MICIN/AEI/10.13039/501100011033). *(Corresponding author: Carmen Bachiller.)*

Vicente Nova, Carmen Bachiller, Jordi Pascual-Folch, Álvaro Ferrer, and Vicente E. Boria are with Instituto de Telecomunicaciones y Aplicaciones Multimedia (iTEAM) (e-mail: vinogi@iteam.upv.es; mabacmar@dcom.upv.es; jorpasf1@teleco.upv.es; alfercla@iteam.upv.es; vboria@dcom.upv.es). Luis N. Ponce-Gonzalez and M. Luisa Marin belong to Instituto de Tecnología Química (ITQ). Universitat Politècnica de València and Consejo Superior de Investigaciones Cientficas. Camino de Vera, s/n, 46021 Valencia, Spain. (e-mail: lnpongon@posgrado.upv.es; marmarin@qim.upv.es)

bly. Additive manufacturing offers rapid prototyping of high-frequency devices at a reduced mass and cost, particularly for small to medium production volumes where traditional machining is expensive. Previous studies on AM have investigated their use for a wide range of devices [5], [11]–[16]. However, these studies have mainly focused on developing complex geometries, without considering miniaturisation or integration with planar subsystems, factors that limit their use in new satellite communication systems. This work aims to fill this gap by combining additive manufacturing with substrate integration through SMT. The proposed approach could address the design and price limitations of SICs, as well as the interconnection and mass issues of waveguides.

The structure of this paper is as follows. In the first section, we elaborate on the design process of the surface-mount assembly, and its application to the development of SMT filters. Furthermore, we illustrate the design of three SMT cavity filters with different resonator topologies operating at X and C bands. The second section delves into the manufacturing process, covering 3D printing and plating techniques. In the fourth section, we analyse the experimental results and compare them with other related works. In the fifth section, we conduct a deviation analysis investigating the effect of the different manufacturing tolerances on the performance of the filters. Section six explores the manufacturing issues. Lastly, our conclusions are drawn in section seven.

II. Electromagnetic Analysis and Design

A. Surface-Mount Technology

The proposed surface mounting assembly is shown in Fig. 1 (a), (b), and (c), where the layout of the different filter topologies is depicted. Filters lay on a PCB that serves as a metal lid and transition between them and the microstrip lines (MSLs). The proposed transition consists of a narrow slot aperture performed on the ground plane of the MSL. The slot cuts the MSL current return path, behaving as a magnetic monopole that excites the preferred mode of the 3D-printed waveguide [17], [18].

The performance of the slot transition depends on its dimensions, position and orientation. In order to maximise the power transfer, the slot should be placed perpendicular to the MSL at a location where the magnetic field is maximum in both the MSL and the waveguide [18]. This can be achieved by short-circuiting the MSL at the slot position or using an open-ended stub with a length of one-quarter wavelength. In this study, the latter configuration was chosen as it does not require plated-through holes, which would increase the radiation loss and need additional manufacturing processes. The position of the slot in the waveguide depends on the preferred mode, but as a general guideline, the separation between the slot and the vertical wall of the waveguide (d) should be minimised [17], [19]. Considering these recommendations, the working frequency and bandwidth of the transition can be easily controlled by adjusting the length and width of the slot.

In this work, the slot structure was used as the input/output (I/O) coupling element of the proposed filters, eliminating the need for additional feeding waveguides and coupling windows. Moreover, the coupling slot does not need complex planar transitions that tend to be challenging to design, and typically require non-standard PCB manufacturing techniques [20], [21]. Thus, this approach reduces the device length and simplifies the design process, addressing the main limitations and drawbacks of traditional integrated filters (SIW and Empty SIW -ESIW-), and eases the integration of complex 3D geome-

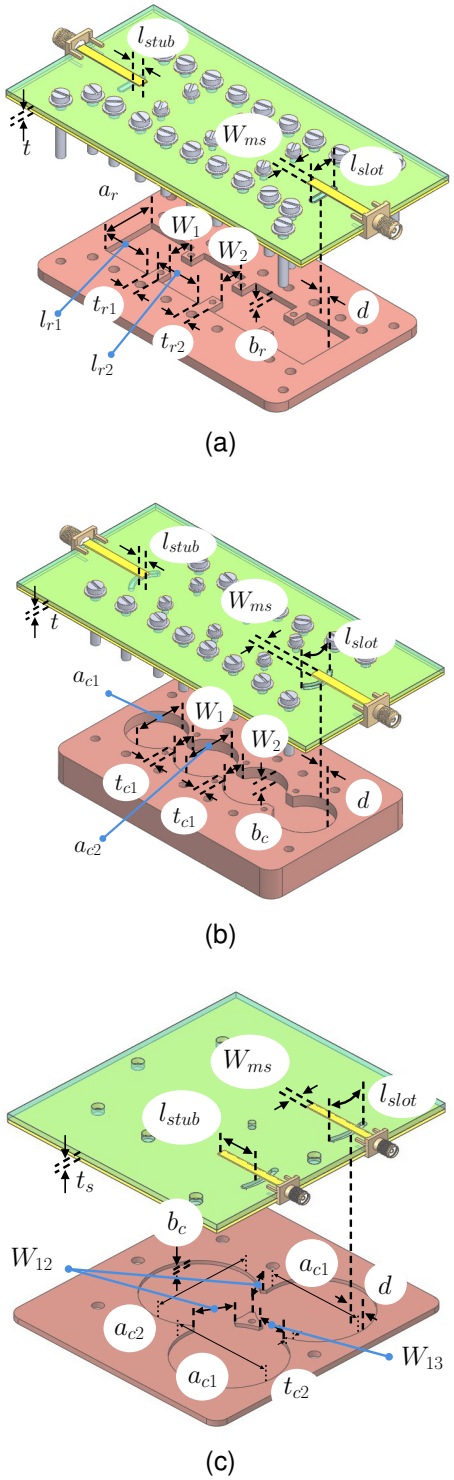

Fig. 1. Assembly of the three SMT filters. (a) 3D view of the X-band rectangular cavity filter. (b) 3D view of the X-band circular cavity filter. (c) 3D view of the C-band tri-section filter.

tries with planar subsystems.

B. Filter Design

In this work, three waveguide filters with bandpass responses have been designed and manufactured to benchmark the RF performance of the proposed approach, in particular:

- An in-line filter centred at 11 GHz (X band) based on rectangular cavities, as shown in Fig. 1 (a).
- An in-line bandpass filter centred at 11 GHz (X band) based on circular cavities, as shown in Fig. 1 (b).
- A triplet bandpass filter centred at 5.25 GHz (C band) based on circular cavities, as shown in Fig. 1 (c).

The filters were designed following the coupling matrix synthesis method, as described in [22]. The design process begins by generating the rational polynomials of the filter response. Next, the transversal coupling matrix is computed and re-arranged to obtain a coupling matrix for the desired filter topology [23]. Finally, the ideal coupling elements and resonators are related to the physical dimensions of the filter structure by using a full-wave electromagnetic simulator.

The design procedure starts by determining the dimensions of the filters' cavities, so they resonate at the desired frequency. The proposed cavities were designed to operate at their respective fundamental modes: the TE_{101} for the rectangular cavity and the TM_{010} for the circular one. The dimensions of these cavities can be easily calculated as specified in (1) and (2).

$$f_{TE_{101}} = \frac{c_0}{2\pi}\sqrt{\left(\frac{\pi}{a_r}\right)^2 + \left(\frac{\pi}{l_r}\right)^2} \tag{1}$$

$$f_{TM_{010}} = \frac{c_0}{2\pi}\left(\frac{2P_{01}}{a_c}\right) \tag{2}$$

, where c_0 is the speed of light, a_r and l_r are the width and length of the rectangular resonator, a_c is the diameter of the circular cavity, and P_{01} is the first zero of the Bessel function of zero kind.

As can be noticed, the resonant frequency of both resonant modes is independent of the height, so it can be chosen based on requirements of compactness, quality factor or spurious mode rejection. Resonators with low height should be chosen when compactness is an essential requirement. In contrast, high-height resonators should be used when a high-quality factor is needed, for instance, for developing narrow bandpass filters.

After determining the dimensions of the ideal resonators, the dimensions of the inter-resonator couplings structures should be adjusted to obtain the proper coupling values. For this purpose, we can determine the coupling factor M from the numerical simulation of two coupled resonators by (3).

$$M = \frac{f_0}{BW}\frac{f_1^2 - f_2^2}{f_1^2 + f_2^2} \tag{3}$$

, where f_0 and BW are the centre frequency and bandwidth of the bandpass filter response, and f_1 and f_2 are the higher and lower resonant frequencies of the two coupled resonators.

Similarly, the external quality factor Q_{ext} needed to implement the desired filter response can be approximated from the simulation response of a single-loaded resonator using (4).

$$Q_{ext} = \frac{\omega_0 \tau_{(\omega_0)}}{4} \tag{4}$$

, where $\tau_{(\omega_0)}$ is the group delay of the simulated S_{11} parameter at the centre frequency.

After designing all the coupling elements, the resonators are fine-tuned, and the completed filter structure is simulated and optimised to achieve the desired filtering response.

C. X-Band Filters

This section presents two practical realisations of a 4-pole Chebyshev bandpass filter, which is centred at 11 GHz, with a bandwidth (BW) of 300 MHz and 20 dB of return loss (RL). The required coupling coefficients M and external quality factors Q_{ext} are: $Q_{\text{X-band}} = 34.22$, $M_{12,X} = M_{34,X} = 0.911$ and $M_{23,X} = 0.700$.

The layout of the first realisation is shown in Fig. 1 (a). It comprises four WR75 rectangular cavities of width $a_r = 19.05$ mm and initial length of $l_r = 19.5$ mm. In this realisation, a low-height resonator was chosen to reduce the size of the device, and facilitate its integration into planar subsystems. The resonator's height was set to $b_r = 2$ mm, a typical value for substrate-integrated filters (ESIW and air-filled SIW -AFSIW-) [21]. Filter resonators were coupled through inductive irises of thickness $t_r = 4$ mm, so we can place a screw at such position to reduce the radiation loss of the assembling gap.

The second filter realisation comprises four cylindrical cavities connected through inductive irises; see Fig. 1 (b). In this case, high-profile resonators were used to achieve a higher unloaded quality factor. However, higher resonators could degrade the Spurious Free Range (SFR) as the resonance frequency of higher-order modes is reduced. For high a_c/b_c ratios, the dominant mode of the circular resonator is the TM_{010} and the two closest spurious modes are TM_{110} and TE_{111}, whose resonant frequencies can be obtained from (5) and (6).

$$f_{TM_{110}} = \frac{c_0}{2\pi}\left(\frac{2P_{11}}{a_c}\right) \tag{5}$$

$$f_{TE_{111}} = \frac{c_0}{2\pi}\sqrt{\left(\frac{2P'_{11}}{a_c}\right)^2 + \left(\frac{\pi}{b_c}\right)^2} \tag{6}$$

, where a_c is the diameter of the cavity, P_{11} and P'_{11} are the first zero of the Bessel function of the first kind and the first zero of its derivative. The resonant frequency of the TM_{110} mode is not sensitive to the resonator height (b_c), but the second spurious mode TE_{111} is. Therefore, as the resonator height increases (lower a_c/b_c ratios), the resonant frequency of the TE_{111} mode decreases, and the spurious-free range is accordingly degraded. The maximum height of the cavity (b_c^{MAX}) is that at which the resonant frequencies of both spurious modes (TM_{110} and TE_{111}) have similar values so that it can be reduced to (7).

$$b_c^{MAX} = \frac{a_c \pi}{2\sqrt{P_{11}^2 - (P'_{11})^2}} \quad (7)$$

The maximum height for the proposed resonator is about 9.80 mm, but a height of $b_c = 10.00$ mm was chosen for simplicity. In this filter implementation, the thickness of the coupling irises was set to 3.00 mm, since the circular shape of the resonators facilitates fixing screws at such positions. In addition, thicker irises have to be wider to obtain the same coupling coefficient, which results in a narrower SFR.

Both filters were externally coupled to a 50 Ω microstrip line ($W_{ms} = 3.25$ mm) through the proposed slot transition, which was implemented on a RO4003C substrate with relative permittivity of $\varepsilon_r = 3.50$, a thickness of 1.524 mm and a copper cladding of 17μm. In order to get the required coupling factor for the filters, some transition dimensions were fixed: $t_{slot} = 0.7$ mm and $d = 2.35$ mm for the rectangular filter, and $t_{slot} = 0.8$ mm and $d = 2.5$ mm for the circular filter. Otherwise, a value of $l_{stub} = \lambda/4 = 3.57$ mm was chosen for both resonators as a starting point and then optimised.

The external quality factor and coupling elements of both filters were extracted using the method described in the previous section. Fig. 2 (a) shows the extracted Q_{ext} of both filters versus the slot length l_{slot}, and Fig. 2 (b) shows the extracted internal coupling coefficients of the inductive irises versus their width W.

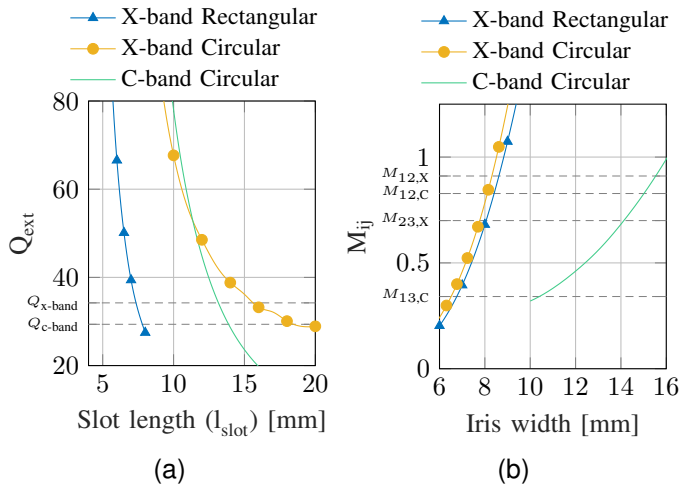

Fig. 2. Extracted coupling elements for X- and C-band filters. (a) External quality factor as a function of the slot length. (b) Inter-resonator coupling vs iris width.

Both filters were finally simulated and optimised using CST Studio Suite (v.2021, CST GmbH, now with Dassault Systèmes), obtaining the dimension values listed in Table I, and the simulated responses shown in Figs. 6 and 7.

D. C-Band Filter

Another bandpass filter, whose response is centred at C band, has been designed to evaluate the feasibility of the proposed approach at different frequencies and with other filter topologies. In particular, a tri-section filter centred at 5.25 GHz with an equi-ripple bandwidth of 200 MHz, 15 dB of return loss (RL) and a transmission zero (TZ) located at 5.492 GHz has been designed. With the given specifications, the required external quality factor and coupling coefficients are $Q_{\text{C-band}} = 29.364$, $M_{11,C} = M_{33,C} = 0.075$, $M_{22,C} = -0.370$, $M_{12,C} = M_{23,C} = 0.828$, and $M_{13,C} = 0.341$. The filter response covers the low-power Unlicensed National Information Infrastructure (U-NII)-1/2 bands [24], and the high-frequency rejection provided by the TZ is of interest for the 5 GHz WLAN standard.

TABLE I
MOST IMPORTANT DIMENSIONS OF THE THREE FILTERS.

Rectangular X-band filter		Circular X-band filter		Circular C-band filter	
Parameter	**Value (mm)**	**Parameter**	**Value (mm)**	**Parameter**	**Value (mm)**
l_{stub}	3.579	l_{stub}	3.950	l_{stub}	8.600
d	2.350	d	2.500	d	3.000
l_{slot}	6.952	l_{slot}	13.796	l_{slot}	14.269
l_{r1}	17.424	a_{c1}	20.475	a_{c1}	41.674
l_{r2}	16.883	a_{c2}	20.085	a_{c2}	41.960
W_1	8.187	W_1	8.228	W_{12}	14.577
W_2	7.749	W_2	7.771	W_{13}	11.235

Since the electric response of the filter is asymmetric, resonators are not synchronously tuned, being $f_{res1} = f_{res3} = 5.242$ GHz and $f_{res2} = 5.286$ GHz. For these specifications, the initial diameter of the resonators is 21.88 mm for resonators 1 and 3, and 21.71 mm for the second resonator. The height of the resonators, b_c, was chosen as 1.524 mm to allow its comparison with filters that have already been designed in the same band.

The proposed filter was coupled to the same MSL designed for the X-band filters, and the inter-resonators couplings were also implemented through inductive irises, as can be seen in Fig. 1 (c). The dimensions of coupling elements were optimised following the same procedure as for the X-band filters. Fig. 2 (a) depicts the curve of the Q_{ext} values as a function of the l_{slot}, the other sizes of the transition are $l_{stub} = 8.6$ mm, $t_{slot} = 1.25$ mm and $d = 3$ mm. Fig. 2 (b) shows the coupling coefficient as a function of the iris width W, being $t = 2$ mm the thickness of the iris. The filter response was finally optimised, obtaining the dimensions listed in Table I, and the simulated response shown in Fig. 8.

III. Manufacturing Procedure

A. Additive Manufacturing of Microwave Devices

Filters were fabricated with a stereolithography (SLA) Form 2 printer from Formlabs [25]. This printer was chosen for its high resolution (about 80 μm), high dimensional accuracy ($> 25\mu$m), and relatively low price (approximately 4000 US$ when it was launched). Moreover, the SLA technique is known to achieve the best surface finishing among commercial desktop AM techniques, which makes it particularly suitable for microwave and mm-wave devices.

3D printing is a complex process when dimensional accuracy is critical, as there are several factors involved in deformation processes that ultimately impact the dimensional accuracy of the printed part. There are two main sources of

deformation in SLA technology: the adhesion of the freshly printed layer with the film of the resin tank or vat, and the shrinkage of the resin during printing and post-processing processes.

The adherence of the freshly printed layer with the vat film can be strong enough to cause deformations. However, it can be simply minimised by selecting a proper printing orientation and support structure. A correct printing orientation reduces the contact area between the last solidified layer and the vat film, reducing the adherence strength and hence the deformation forces. Additionally, a densely distributed support structure can efficiently sustain distant areas of the layer, reducing their associated distortion. Most commercial slicing software already optimises these parameters, although the help of an experienced operator may be needed.

In all polymeric printing techniques, the resin shrinks during the hardening and bonding process, which induces stress between the layers of the printed parts that leads to deformations and warps. This deformation mechanism is quite complex, since it depends not only on the material properties but also on the part geometry and its printing orientation. Thus, the more straightforward solution to minimise this effect is to use a low-shrinkage resin. Unfortunately, resin manufacturers do not generally provide this information, and although there are studies that address this issue [26], [27], there is no information available for all resins. After numerous printing experiments, we observed that composite resins with a high quantity of solid particles have a significantly lower shrinkage than pure polymeric ones. This is because solid particles of the resin do not change their size during the printing process [28]. For these reasons, prototypes in this work were printed using the Rigid 10k resin from Formlabs, a resin filled with a 55-75% of silica (SiO_2). While this resin helped reduce deformation caused by shrinkage, it did not completely eliminate it. The shrinkage still caused significant deformation in very flat parts, i.e., rectangular X-band filter and the C-band filter. Similar deformations were also observed in flat groove gap structures [29]. As a solution, a honeycomb reinforcement structure was added to these flat prototypes to distribute the deformation forces more evenly [30].

Finally, all parts were orientated in the printing platform so that their maximum layer area was minimised and no supports were needed in critical surfaces, such as the surface of the cavities and the contact surfaces between PCBs and filters.

After printing, parts were cleaned in isopropyl alcohol to eliminate unsolidified resin, and they were cured for 1 hour in a UV lamp to finish the hardening process. Afterwards, they were heated at 125°C for 90 min to enhance the mechanical and thermal properties of the Rigid 10K resin employed.

B. Plating Process

Once the device is printed and hardened, it should be plated with a homogeneous layer of an electrically conductive material. This is commonly done by using two successive plating processes. The first one involves the deposition of a thin conductive layer, which is used to apply a last electroplating for covering minor defects, thus thickening and stabilising the already deposited metal coating.

Regarding the first plating process, there are three commonly used methods: Physical Vapor Deposition (PVD), electrically conductive paints, and electroless plating. Conductive paints are by far the simpler method, since it consists of applying a conductive paint over the printed part. This technique achieves an extremely high adhesion, since some painting solvents can dissolve part of the printed polymer bounding it to the paint. However, the painting coating tends to be inhomogeneous and has very low electrical conductivity. In contrast, PVD allows the coating of a wide range of materials, obtaining a highly conductive coating with high adherence. While this method is very convenient for plating flat substrates, it provides a non-homogeneous coating in arbitrary-shaped geometries and needs for high-cost and high-energy-consuming processes [31], [32]. Contrary, electroless plating can homogeneously plate arbitrary-shaped parts in a cheap and simple manner, and provides a large flexibility of volume production.

In this work, the first coating was applied by using copper electroless plating. This method utilises a chemical reaction to attach copper particles to the surface of polymeric samples without the use of an electric current [33]. In order to do so, the sample surface must be prepared to allow a strong bond with the metal deposition. Then, a catalytic layer is deposited on the part surfaces. This layer is responsible for starting the chemical reaction in which the metal, copper in this case, is attached to the surface. While this process has been used in previous works, an optimisation study was conducted to tailor it to the Rigid 10K resin. To the best of our knowledge, this is the first time that it was successfully applied to the Rigid 10k resin. The optimised process for this material is as follows:

1) Etching: polymer surfaces generally have a low wettability, meaning they have few sites for binding to metal coatings. The most common method to increase the surface wettability involves a chemical etching with strong oxidising compounds such as chromium salts. However, this product is not recommended because it is highly corrosive and pollutant. In this work, the chromium salt etching was replaced by combining a first shot blasting, and a subsequent chemical etching using a sodium hydroxide solution. The shot blasting was performed with a 60 grit white corundum, and the chemical etching consisted of $1g/100mL$ of sodium hydroxide ($NaOH$) in a solution of ethyl alcohol and distilled water with a volume ratio of 1:1. After shot blasting, parts were immersed in this solution at 50°C during 10 min under continuous magnetic stirring. This process is much less dangerous and pollutant than traditional processes, cutting costs associated with safety and waste management [34].
2) Activation: this step consists in immersing the part in an aqueous solution of 0.25 g/L of $PdCl_2$, 12 g/L of $SnCl_2$ and 60 mL/L of 38% HCl at 25°C for 5 min under continuous magnetic stirring. This phase achieves the attachment of a thin layer of a palladium-tin alloy that acts as a catalyst for the subsequent copper deposition reaction.

3) Acceleration: the presence of tin on the catalytic surface can interfere with the coating reaction. Therefore, it is crucial to remove this material using a solution that exposes the palladium atoms to the final autocatalytic bath. This is achieved by immersing the activated sample in an acid solution containing 32 mL/L of 38% HCl at 25°C for 5 minutes under continuous magnetic stirring.
4) Copper deposition: the part is finally immersed in a copper-formaldehyde solution at 46°C for 15 minutes under air flow and continuous magnetic stirring. In this phase, the catalytic sites start the reduction reaction of the copper solution, giving rise to the copper layer.

The initial plating process results in a relatively uniform and stable copper deposition, although it may leave some small areas uncovered, particularly in sharp corners. An additional electroplating process is applied to address these minor defects, producing a thicker and more uniform layer of copper. The electroplating was performed using the MiniContact-RS commercial plating system from LPKF [35].

Field Emission Scanning Electron Microscopy (FESEM) images have been taken to evaluate the thickness of the copper cladding resulting from each step. For this purpose, a trench was performed at different metallisation stages, and different accelerating voltages were used to capture the images. Lower accelerating voltages produce less penetration in the sample but higher resolution, while higher accelerating voltages produce more penetration but lower resolution. Fig. 3 (a) shows a layer of 0.5 to 1.7 μm upon the electroless plating, while the final copper layer upon the second stage (Fig. 3 (b)) was smoother and thicker (6.5 to 12 μm).

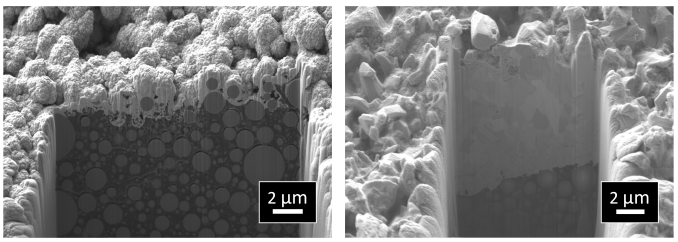

Fig. 3. FESEM view of a trench performed on the metallised polymeric device with Gallium Focused Ion Beam (Ga+ FIB). Accelerating voltages of 2 kV and 3 kV were used to capture images (a) and (b), respectively. The copper layer (in white) is on top of the polymeric material (light grey are particles of SiO_2). (a) After the electroless metallisation. (b) After the galvanic metallisation.

C. PCB Processing and Assembling

PCBs were manufactured using a Protomat 103s milling machine from LPKF. The 3D-printed parts and PCBs were fastened and assembled without the use of soldering, which reduces the material and assembling costs. Photographs of the manufactured filters can be seen in Fig. 4.

IV. Results

Filters were measured using a Vector Network Analyser (VNA) and the proper SMA connectors. Measurements were done using a specific microstrip TRL calibration kit that allows a full two-port calibration of the measurement setup. The TRL calibration kit locates the reference plane at 7 mm from the slot, see Fig. 4, which eliminates the detrimental effect of SMA connectors and feeding lines on the measured results. The custom through, line and open standards used in the calibration kit can be seen in Fig. 5.

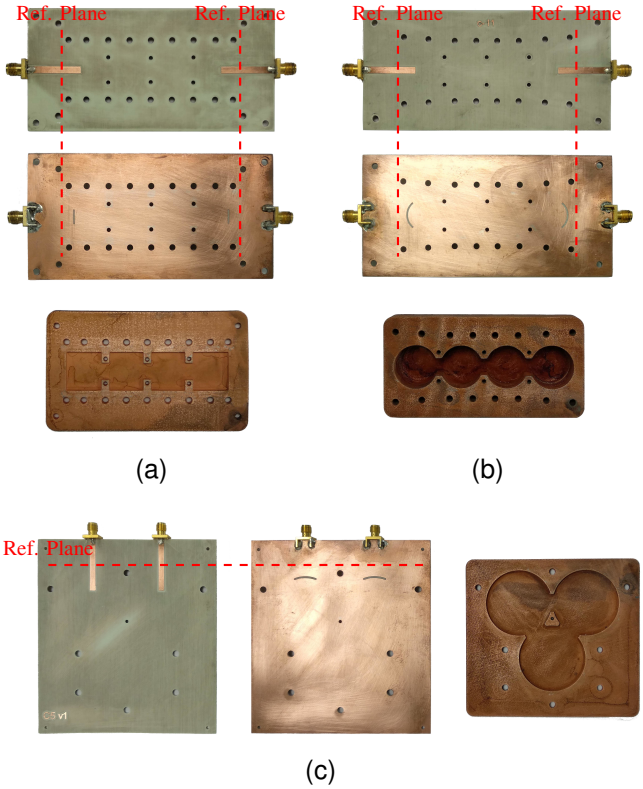

Fig. 4. Photographs of the manufactured filters: a) Rectangular X-band filter, b) Circular X-band filter, c) C-band tri-section filter.

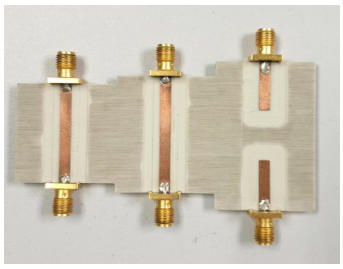

Fig. 5. TRL standards. From left to right: Through, Line, and Open.

Fig. 6 shows the frequency response of the rectangular X-band filter. The measurement results are in reasonable agreement with the simulation. The filter has a centre frequency of 10.947 GHz, with a centre frequency deviation of -57 MHz (-0.4 %), and a 3-dB bandwidth variation of 45.3 MHz (15.1%). The average insertion loss in the passband is 2 dB, which is approximately 1.5 dB higher than for the simulated results.

Fig. 7 shows the frequency response of the circular X-band filter. The measurement results show a mid-band insertion loss of 1.75 dB, which is 1.25 dB higher than the simulated values.

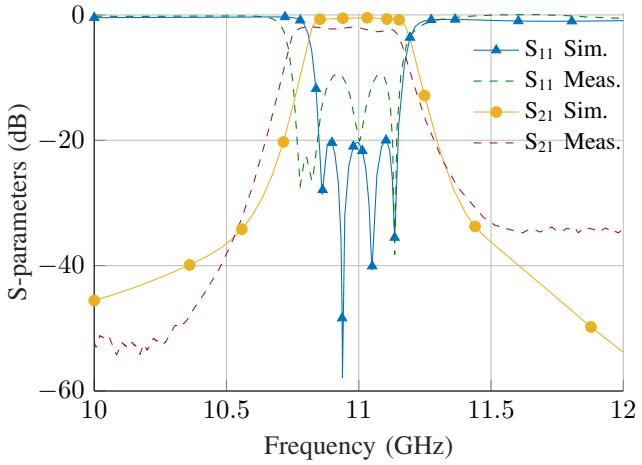

Fig. 6. Measured (dashed) and simulated (solid) response of the rectangular X-band filter.

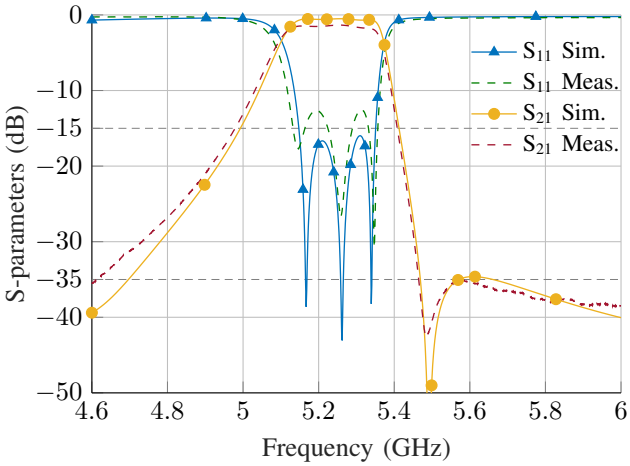

Fig. 8. Measured (dashed) and simulated (solid) response of the C-band tri-section filter.

The centre frequency deviation is minimal (-2.2 MHz, i.e., -0.02%), and the measured 3-dB bandwidth deviation is 16 MHz (4.2%).

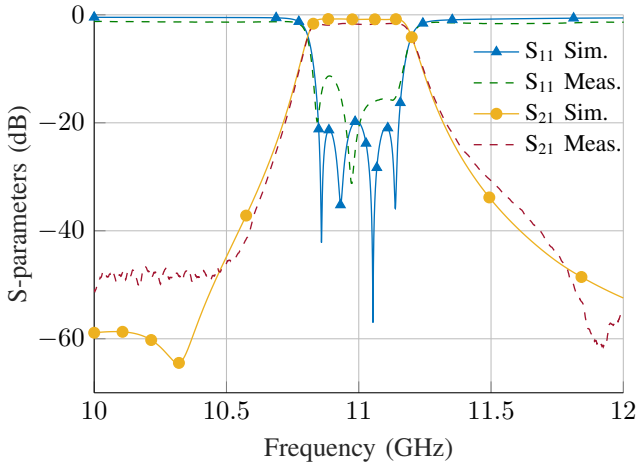

Fig. 7. Measured (dashed) and simulated (solid) response of the circular X-band filter.

The measured response of the C-band filter is presented in Fig. 8. The measured results exhibit an in-band insertion loss of 1.43 dB, which is slightly higher than the expected value. The deviation of the centre frequency is 24 MHz (0.46%), and the deviation of the measured 3-dB bandwidth is 13.7 MHz (5.10%).

The measured IL of all filters is considerably higher than simulated data. This is probably due to several factors that were not considered in simulations, such as the oxidation of the copper, the effect of surface roughness in the ohmic loss, and the radiation loss produced in the assembling gaps between PCBs and filters. These effects will be further studied in sections V and VI.

It is also noteworthy that the out-of-band responses of both X-band filters differ from the ideal response. The upper band rejection of the X-band rectangular filter is lower than the simulated one, which can be attributed to a parasitic input/output coupling caused by the assembling gap and the orientation of the filter's feeding lines. A similar effect can be observed in the lower band rejection of the circular X-band filter. Since the open-ended microstrip lines are placed opposite each other in the X-band filters, the signal can be easily transmitted from one line to another, promoting this parasitic coupling. This effect can be mitigated by altering the MSL orientations, as was done for the C-band filter, where this parasitic coupling was eliminated. However, feeding lines were not re-designed for the X-band filters, since the obtained attenuation level is high enough for most practical applications.

In Table II, filters proposed in this work are compared to similar additively manufactured filters. Our X-band realisations exhibit comparable IL values to monolithic filters manufactured using SLM printing technology. However, the filters printed with SLA demonstrate lower IL values than our filter realisations. In the case of the C-band filter, it exhibits slightly higher IL than the state-of-the-art examples. Nevertheless, the filters proposed in this work feature a significantly reduced footprint, comparable only with multimode filters [36]–[38]. Additionally, they are easily integrated into planar systems through the SMT transition, which makes them attractive for practical applications where size, weight, and integration are critical factors.

In Table III, the filters developed in this work are compared to other SMT and substrate-integrated filter realisations with similar responses. Our proposed filters demonstrate moderate loss values when compared to filled substrate-integrated filters. Additionally, the proposed filters have a similar footprint and insertion loss compared to empty substrate-integrated structures. Our SMT transition design enables easy integration with planar systems without the need for complex transitions or soldering. Furthermore, 3D printing offers unprecedented design flexibility and reduces manufacturing costs compared to substrate-integrated circuits.

V. Tolerance Analysis

Several Monte Carlo (MC) studies were carried out to identify the most critical sources of dimensional deviations

in the manufacturing process. For this purpose, the most representative dimensions of the X-band filters were randomly varied using non-truncated normal distributions.

A first set of 100 simulations studies the tolerances for the PCB machining, assuming a standard deviation of $\sigma = 0.01$ mm for the most crucial dimensions of PCBs: the MSL width W_{ms}, the length of the MSL stubs l_{stub}, the separation between the slots and the short-circuited wall of the input/output resonators d, and the width and length of the slots, t_{slot} and l_{slot}. In this first analysis, the filter responses were almost unaffected, and the worst deviation was observed in the RL, with a maximum variation of less than 1dB.

Then, a second MC analysis was carried out by considering dimensional deviations in both the PCB machining and 3D printing. In this case, 200 simulations were conducted considering the PCB dimensions from the previous study and the filters' dimensions listed in Table I. The standard deviation observed in [49] was taken as a good approximation for our manufacturing setup, being $\sigma = 0.03$ mm for details smaller than 9 mm, $\sigma = 0.04$ mm for dimensions between 10 and 20 mm, and $\sigma = 0.055$ mm for dimensions with values between 30 and 45 mm. As in the previous analysis, a standard deviation of $\sigma = 0.01$ mm was used for the PCBs dimensions. The analyses for the X-band filters are shown in Fig. 9 and 10.

The manufacturing tolerances slightly affect the centre frequency and bandwidth of both filters. However, the small deviations considered in this analysis affect the position of the filters' poles, which increases the minimum RL level in the passband. It is worth mentioning that the rectangular filter seems to have a lower deviation in terms of RL than the circular realisation. However, the measurements of this filter

TABLE II
COMPARISON OF PUBLISHED FILTERS (WITH ADDITIVE MANUFACTURING TECHNIQUES) AT SIMILAR FREQUENCIES.

Ref.	**[36]**	**[39]**	**[37]**	**[40]**	**This work**	**This work**	**[38]**	**[41]**	**[42]**	**This work**
Manufacturing technique	3D-SLA	3D-SLA	3D-SLM	3D-SLM	3D-SLA	3D-SLA	3D-SLM	3D-FDM	3D-FDM	3D-SLA
Filter technology	Spherical	Spherical	Spherical	Triangular	WR	WC	Spherical	WR	Ridge	WC
Feeding line	WR90	WR75	WR90	Coaxial	MSL	MSL	WR-112	WR159	I-MSL	MSL
SMT assembly	No	No	No	No	Yes	Yes	No	No	No	Yes
f_0 **[GHz]**	10	10	11.5	11	11	11	8.23	5.45-5.89	5.45	5.25
FBW [%]	3	5	0.47	1.82	2.73	2.73	5.6	3.93	55	3.8
Filter technology	Spherical Multi.	Spherical Mono.	Spherical Multi.	Triangular Mono.	WR Mono.	WC Mono.	Spherical Multi.	WR Mono.	Ridge -	WC Mono.
IL [dB]	0.25	0.15	1.5	1.75	2	1.43	0.4	2.9-1.6	0.89	1.43
Footprint mm^2	2280	6800*	1500*	3300	1550	1800	4500*	8256	3000*	6500
Height [mm]	31	30*	30*	30	4.5	12.5	31	40.4	5.8*	4

* Estimated values.
(WR) Rectangular Waveguide.
(WC) Circular Waveguide.
(Multi.) Multimode.
(Mono.) Monomode.
(I-MSL) Inverted MSL.

TABLE III
COMPARISON OF PUBLISHED FILTERS (SMT AND SIC REALISATIONS) AT SIMILAR FREQUENCIES.

Ref.	**[43]**	**[44] Filt. 1 / Filt. 2**	**[21]**	**[21]**	**This work**	**This work**	**[45]**	**[46]**	**[47]**	**[48]**	**This work**
Manufacturing technique	PCB	PCB	PCB	PCB	3D-SLA	3D-SLA	PCB	PCB CNC	PCB	PCB	3D-SLA
Filter technology	DE-ESIW	HM-SIW SIW	ESIW	SIW	WR	WC	SIW	Combline MSL	SIW	SIW	WC
Feeding line	MSL	MSL	MSL	MSL	MSL	MSL	MSL	MSL	MSL	CPW	MSL
SMT assembly	No	No	No	No	Yes	Yes	No	Yes	No	No	Yes
f_0 **[GHz]**	11	9/9	11	11	11	11	8	4	5.8	5.25	5.25
FBW [%]	3	3.9/4.4	2.73	2.73	2.73	2.73	3.35	6.25	2.1	3.8	3.8
Filter order	4	3/3	4	4	4	4	5	6	4	3	3
IL [dB]	2.15	2.13/1.73	0.9	2.5*	2	1.43	2.15	9*	3.2	1.5	1.43
Footprint mm^2	1090*	2570*/2450*	1660*	430*	1550	1800	-	361	1200*	1880*	6500
Height [mm]	2.5*	0.6*/0.6*	4.6	1.5*	4.5	12.5	1*	5	2*	1.5*	4

* Estimated values.
(WR) Rectangular Waveguide.
(WC) Circular Waveguide.
(DE-ESIW) Dielectric Element in an ESIW.
(HM-SIW) Half-mode SIW.

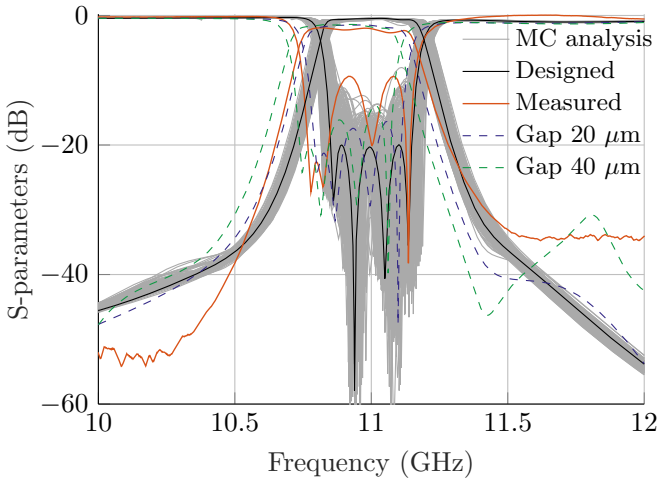

Fig. 9. Tolerance analysis of the X-band filter based on rectangular cavities.

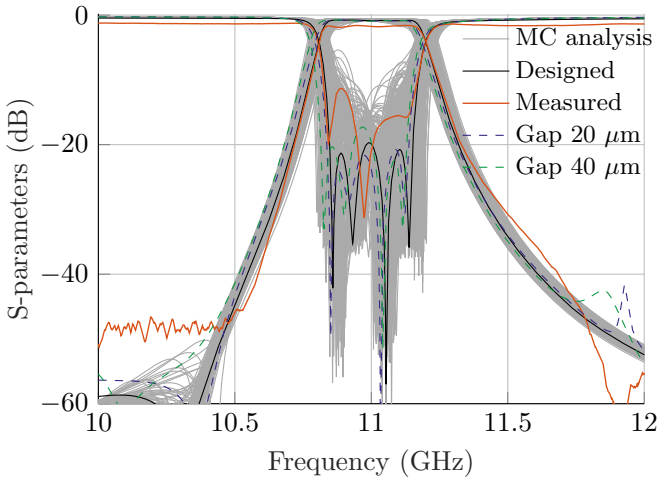

Fig. 10. Tolerance analysis of the X-band filter based on circular cavities.

are not aligned with the MC analysis predictions. This will be discussed further below.

A similar MC analysis considering AM and PCB deviations was performed for the C-band filter. However, the observed deviation in the filter performance was negligible, so this study was not included in this manuscript.

A. Assembling Gap Analysis

Finally, a parametric analysis was conducted in order to study the effect of the assembling gap. Both X-band filters were simulated considering gap thicknesses ranging from 10 to 100 μm. Simulation results for a gap thickness of 20 and 40 μm are shown in Fig. 9 and 10. In general, the gap reduces the centre frequency and increases the insertion loss. The analysis also revealed a linear relationship between the gap thickness and the deviation of the centre frequency of the filters. The rectangular filter shows a centre frequency shift of -2.44 MHz/μm, three times higher than in the case of circular realisation (-0.664 MHz/μm).

Figure 11 illustrates the average loss (including radiation and ohmic losses) within the passband, calculated as $1-(|S_{11}|^2+|S_{21}|^2)$. As can be noticed, there is an exponential relationship between the loss and gap thickness. This exponential curve has a considerably steeper slope in the case of rectangular cavities, whilst circular cavities exhibit a shallower slope. This effect is also apparent in Figs. 9 and 10, where it is evident that the rectangular filter exhibits higher insertion loss for the same gap thickness.

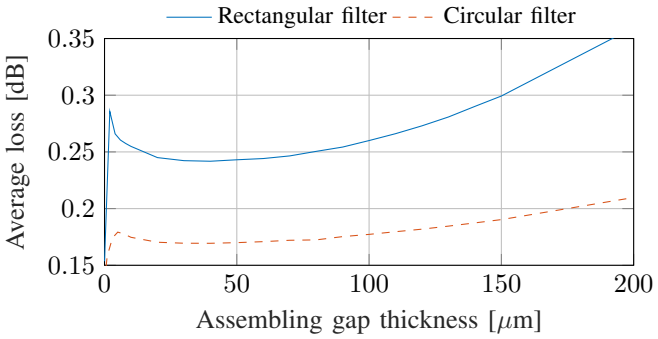

Fig. 11. Evolution of the average loss in the passband relative to the gap thickness.

It should be noted that the assembling gap between the filter body and the PCB also acts as a parallel-plate transmission, which increases the parasitic I/O coupling between the feeding lines, as shown in Fig. 12. Consequently, as the gap thickness increases, the out-of-band rejection levels decrease. This effect is much stronger in the rectangular filter, as can be noticed in Figs. 9 and 10.

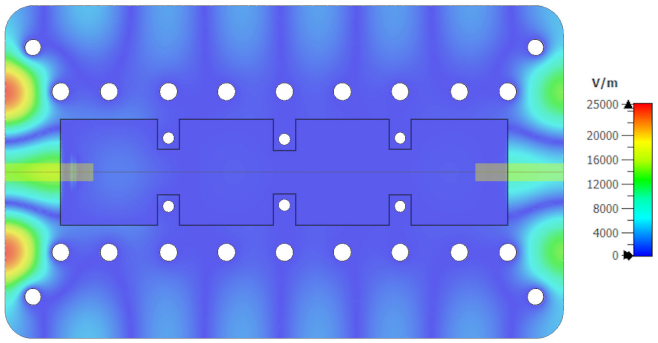

Fig. 12. Electric field distribution at 12 GHz for the rectangular X-band filter with a gap of 50 μm.

Based on the results, it can be inferred that the rectangular filter is noticeably more susceptible to the effects of gaps and mismatches in terms of centre frequency and insertion loss compared to the circular counterpart. This finding helps to partially explain the higher degree of deviation observed in the measurements of the rectangular filter. However, a more detailed analysis of these discrepancies is presented in the following section.

VI. Manufacturing Issues and Material Characterisation

The measurements of the rectangular X-band filter show a significant degradation in its performance, which cannot be

fully explained by the effect of the expected manufacturing tolerances and assembling gaps studied in the previous section. The degradation of this filter should be due to several factors that were not evaluated in the previous analysis. This section examines what factors were overlooked and how they impacted the performance of the filter.

There are several stages in the manufacturing and assembling processes that can negatively affect the performance of the proposed filters:

- Additive manufacturing. Previously presented MC analysis studied the effect of manufacturing tolerances on the filters performances. However, in the case of polymeric printers, such as SLA, accurately defining manufacturing tolerances can be challenging due to factors like material shrinkage, which depends on the part geometry. Although we have taken several measures to reduce the expected warping, it could still be a significant issue. Additionally, the surface roughness of additively manufactured parts can increase ohmic loss in high-frequency devices, which can explain some of the discrepancies in terms of IL values.
- Polishing. Additively manufactured parts were sand-blasted in order to improve the copper adhesion. However, this process removes a layer of the surface, increasing the size of the parts' cavities, and altering the resonant frequency to lower values. Additionally, this erosion may not be homogeneous, leading to higher dimensional deviations.
- Plating. The plating process deposits a thin layer of copper on the surface of the device. Our dimensional analysis shows a thickness range of 6.5 to 12 μm, which can affect the final dimensions of the filters. This was not considered during the design process, since deviations in this order have a minor impact on the filter's performance. On the other hand, the deposited copper layer can oxidize over time, reducing its effective conductivity.

In conclusion, two main factors cause the deviation in the filter response. Firstly, the part geometry may have a greater dimensional deviation than anticipated, probably due to a substantial part deformation. Secondly, it appears that copper oxidation and surface roughness may have a more significant impact on ohmic losses than was expected. In the following sections, these two factors will be further investigated.

A. *Effective Conductivity Characterisation*

Next, the RF performance of the copper deposition is evaluated using a 3D-printed rectangular cavity resonator. This approach allows to define an effective electrical conductivity that consider the real conductivity of the oxidised copper, and the effect of the surface roughness.

The proposed resonator is based on a rectangular cavity with a =19.05 mm of width, b =9.53 mm of height, and l =18.46 mm of length operating at 11 GHz. The cavity is excited by inductive irises, and it is fed by standard WR75 waveguides with UBR120 flanges. The resonator was manufactured in a clamshell configuration, see Fig. 13, minimising the radiation losses caused by the assembling gaps. Both parts of the resonator were printed in similar conditions to the filters presented in this work: using the same material, printing orientation and post-processings, so it has similar roughness and oxidation finishing.

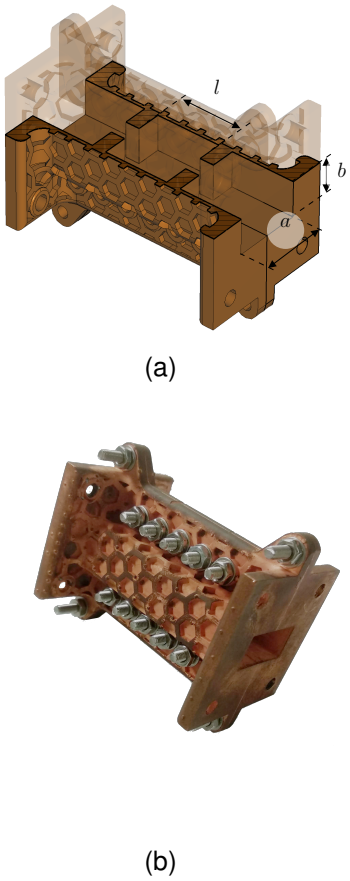

Fig. 13. High-quality resonator used to extract the effective conductivity of the copper coating. (a) Layout with most important dimensions. (b) Photo of a manufactured resonator.

The loaded quality factor (Q_L) was extracted from the measured transmission coefficient (S_{21}) using the equation describe in [22], $Q_L = \frac{f_0}{\Delta f_{-3dB}}$, where f_0 is the resonance frequency and Δf_{-3dB} is the 3-dB bandwidth. The external (Q_{ext}) and unloaded (Q_u) quality factor were computed with the well known expressions (8) and (9), respectively.

$$Q_{ext} = \frac{Q_L}{S_{21Max}} \tag{8}$$

$$\frac{1}{Q_u} = \frac{1}{Q_L} - \frac{1}{Q_{ext}} \tag{9}$$

Afterwards, the Q_u was used to compute the effective electric conductivity, using the expression of the quality factor of an isolated TE_{101} cavity resonator, and the equation for the conductivity of a good conductor, which read as:

$$R_s = \frac{(kal)^3 b\eta}{Q_u 2\pi^2} \times \frac{1}{2a^3b + 2bl^3 + a^3l + al^3} \tag{10}$$

$$\sigma_{eff} = \frac{2\pi f \mu_0}{2R_s^2} \tag{11}$$

, where R_s is the surface resistivity, k is the wavenumber, σ_{eff} is the effective conductivity, and a, b and l are the width, height, and length of the cavity, respectively.

Then, a more accurate result was obtained by matching the measurement results to simulations using CST. The optimisation process started from the conductivity computed from (10) and (11). Table IV summarises the measured resonance parameters and related conductivity of two different realisations of the proposed resonator. The dimensions of the first resonator are $a = 19.00$ mm, $b = 9.33$ mm, and $l = 18.35$ mm, while the second resonator has dimensions of $a = 19.05$ mm, $b = 9.53$ mm, and $l = 18.46$ mm. The effective conductivity was computed and simulated using the measured dimensions.

TABLE IV
RESONANCE FREQUENCY, UNLOADED QUALITY FACTOR, AND EXTRACTED CONDUCTIVITY OF WR75 RESONATORS.

Realisation	**Resonance frequency (GHz)**	Q_u	σ_{eff} **from (10)** (MS/m)	σ_{eff} **from sim.** (MS/m)
Resonator 1	11.049	3906	17.93	18.55
Resonator 2	11.065	3747	15.67	16.87

Both resonators have similar conductivity values, and their difference can be attributed to slight variations in oxidation and surface roughness. Considering both results, the copper coating has an average effective conductivity of 17.7 MS/m, which is 4 to 8 times higher than that reported in other studies that employs similar plating methods [50], [51]. Furthermore, it is 20 times greater than the effective conductivity obtained from binder jetting printed parts infiltrated with copper [52]. It is important to know that the effective conductivity considers the negative impact of oxidation and surface roughness in the ohmic loss. While the effect of roughness in ohmic losses can not be easily compensated, the degradation due to oxidation can be reduced by passivating the copper coating with commercial anti-tarnish treatments, which leaves room for improvement.

B. Dimensional Analysis

The electric response of the rectangular X-band filter exhibits a significant frequency deviation that exceeds the deviations predicted by the tolerance analysis simulations. To understand the cause of this deviation, a series of dimensional analyses were conducted on the filter's most representative dimensions (a, b, l_{r1}, l_{r2}, W_1 and W_2). Measurements were done by using a Rown & Sharpe Global C/I 091208ROWN coordinate-measuring machine, and each dimension was measured at three different positions to reduce the measurement uncertainties.

1) Erosion: We conducted a first dimensional analysis to understand the effect of the shot-blasting process on the X-band filter's dimensions. The measurements were taken before and after the shot-blasting process, and the extracted erosion is presented in Fig. 14. The analysis revealed that the shot-blasting process has a different impact on the dimensions of the cavities and irises. The measurements of the irises protrusions showed a high level of erosion with wide variations, while the erosion in the cavities was relatively consistent, with an average erosion of 0.213 mm and a standard deviation of 0.045 mm. Additionally, it was noted that for most dimensions, such as L_{rn}, a_{rn}, and W_n), the average erosion increases as the value of n increases, indicating that the filter was positioned with its right-hand side closer to the blasting jet during the process.

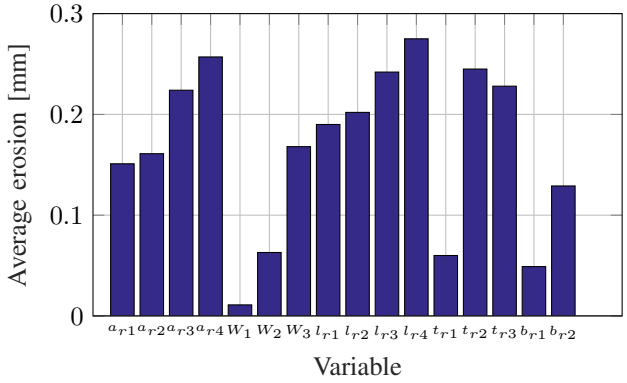

Fig. 14. Average erosion of the shot blasting process.

2) Manufacturing Tolerances: A final dimensional analysis was conducted on the metallised filter. The measurements are included in Table V, and the average deviations with regard to the nominal values are shown in Fig. 15. a and b denote the width and height of the cavities, W and t the width and thickness of the irises, l_1 the length of the first and fourth resonators, and l_2 the length of the second and third resonators.

TABLE V
RESULTS OF THE DIMENSIONAL ANALYSIS PERFORMED ON THE METALLISED FILTER.

Variable	**Value [mm]**	**Variable**	**Value [mm]**
a_{r1}	19.177	W_1	8.333
a_{r2}	19.160	W_3	8.367
a_{r3}	19.170	t_{r1}	4.023
a_{r4}	19.143	t_{r2}	4.040
l_{r1}	17.123	t_{r3}	4.037
l_{r4}	17.133	b_{r1}	1.970
l_{r2}	16.500	b_{r2}	2.000
l_{r3}	16.483	b_{r3}	1.977
W_2	7.903	b_{r4}	1.990

Two systematic errors can be observed. The first error was found in the dimensions representing widths (a and W), which had a high average deviation with similar values, around 120 μm. The second error was observed in the dimensions representing lengths (l_1 and l_2), which showed similar errors of -0.268 and -0.352 mm, respectively, with a more significant variation.

Several factors, such as shrinkage, warping, or the effect of shot blasting can cause the observed deviation in width values. However, the fact that the lengths of the cavities located in the middle of the part (l_2) had a greater error than the exterior ones (l_1), suggests that the error may be due to a slight warping of the part, see Fig. 16. This effect has been observed in similar studies, and tends to occur in very flat parts like the one being studied [29], [30].

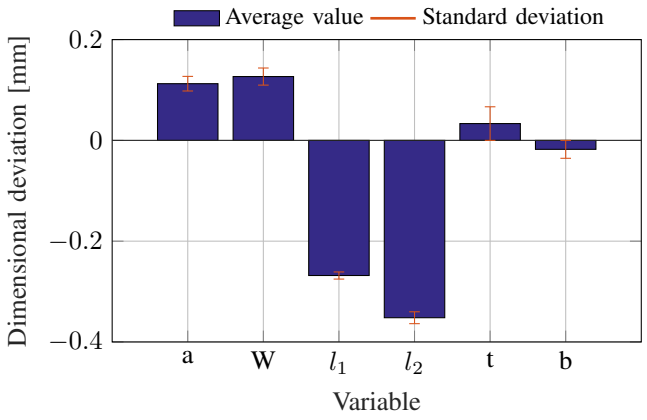

Fig. 15. Average deviations of the metallised filter dimensions.

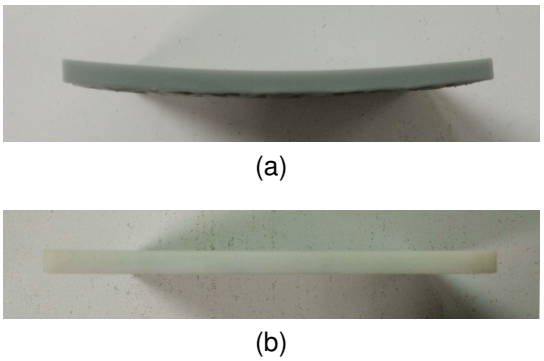

Fig. 16. Warping in rectangular X-band filters printed with different materials. (a) Filter printed with standard SLA resin (Gray) showing noticeable warping. (b) Filter printed with SLA resin Rigid 10K demonstrating a warping reduction. Both filters were printed using the same printing parameters and were subjected to the same post-processing steps.

3) Impact of Manufacturing Issues on the Filter Response: A realistic model of the X-band rectangular filter has been simulated, including the manufacturing issues studied in this section. This model considers a conductivity of 17.7 MS/m for the filter coating, the dimensions specified in Table V, and an assembling gap of 40μm. The assembling gap was determined by measuring the thickness of the PCB and the 3D printed part separately, as well as the total thickness of the assembled filter, using a micrometer screw (Mitutoyo) with an uncertainty of $\pm$ 2 μm. The simulation results are presented in Fig. 17.

The simulation results are in very good agreement with the measurements. Although there is a slight difference in insertion loss, it may be due to slight deviations in dielectric and radiation losses in the PCB. The results of this study indicate that the significant deviation observed in the rectangular X-band filter was a result of higher manufacturing issues, which were likely caused by its highly asymmetric shape. Dimensional measurements of the previous sections can be used in future works to compensate (a priori) for the expected deformation.

VII. Conclusion

This paper has presented a novel approach to developing surface-mount filters using additive manufacturing techniques.

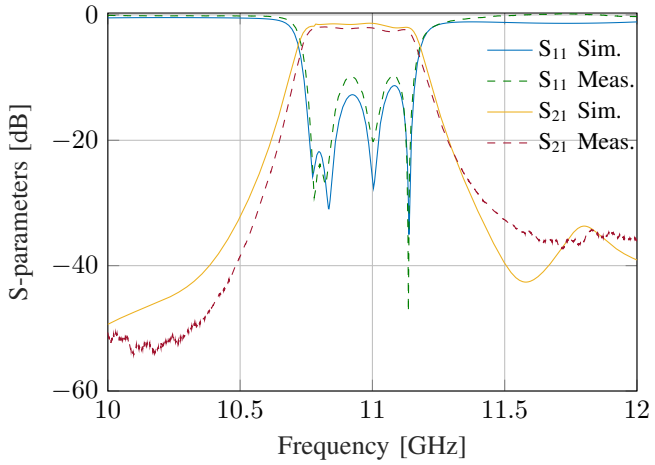

Fig. 17. Realistic simulation of the rectangular X-band filter including all considered manufacturing issues.

The proposed approach offers a simple and reliable integration method that eliminates the need for complex broadband transitions and soldering, providing modularity to the fabricated devices. The employed manufacturing methods, including 3D printing and metallisation techniques, have been described in detail, and their effects on the performance of the filters have been studied comprehensively.

The proposed approach has been successfully applied to bandpass filters with different topologies and operating frequencies. These filters have exhibited similar performance to other 3D-printed filters while presenting a smaller size and weight. Moreover, the SMT assembly enables a straightforward integration with planar circuits, providing an excellent alternative to substrate-integrated filters. Although the proposed filters have a larger footprint than their substrate-integrated counterparts, their superior performance makes them a cost-effective solution when advanced performance and high integrability are required.

The tolerance and dimensional analyses conducted in this study revealed that very flat geometries suffer from higher manufacturing deviations, and circular cavities are more robust against assembling gaps. These findings suggest that circular cavities of high profile are more suitable for the proposed combination of additive manufacturing and SMT assembly.

Altogether, the results of this work demonstrate that the proposed approach is very suitable for developing cavity filters with good performance, offering the advantages of low-cost and lightweight materials, rapid prototyping, and easy planar integration. Finally, the tolerance and dimensional analyses conducted in this study provide valuable insights for future research in the field.

References

[1] B. Al Homssi, A. Al-Hourani, K. Wang, P. Conder, S. Kandeepan, J. Choi, B. Allen, and B. Moores, "Next generation mega satellite networks for access equality: Opportunities, challenges, and performance," *IEEE Commun. Mag.*, vol. 60, no. 4, pp. 18–24, 2022.

[2] C. Ravishankar, R. Gopal, N. BenAmmar, G. Zakaria, and X. Huang, "Next-generation global satellite system with mega-constellations," *Int. J. Satell. Commun. Netw.*, vol. 39, no. 1, pp. 6–28, 2021. [Online]. Available: https://onlinelibrary.wiley.com/doi/abs/10.1002/sat.1351

[3] A. R. Barnes, A. Boetti, L. Marchand, and J. Hopkins, "An overview of microwave component requirements for future space applications," in *Eur. Gallium Arsenide Semiconductor Appl. Symp., GAAS 2005*, Oct. 2005, pp. 5–12.

[4] Chris Daehnick, Isabelle Klinghoffer, Ben Maritz, and Bill Wiseman, "Large LEO satellite constellations: Will it be different this time?" McKinsey & Company, Tech. Rep., May 2020. [Online]. Available: https://www.mckinsey.com/industries/aerospace-and-defense/our-insights/large-leo-satellite-constellations-will-it-be-different-this-time#/

[5] R. Dahle, P. Laforge, and J. Kuhling, "3-D printed customizable inserts for waveguide filter design at X-band," *IEEE Microw. Wireless Compon. Lett.*, vol. 27, no. 12, pp. 1080–1082, Dec. 2017.

[6] K. Wu, D. Deslandes, and Y. Cassivi, "The substrate integrated circuits - a new concept for high-frequency electronics and optoelectronics," in *6th Int. Conf. Telecommun. Modern Satell, Cable Broadcast. Service, 2003. TELSIKS 2003.*, vol. 1, 2003, pp. P–III.

[7] D. Lohinetong, P. Minard, C. Nicolas, J. Le Bras, A. Louzir, J. Thevenard, J. Coupez, and C. Person, "Surface mounted millimeter waveguide devices based on metallized dielectric foam or plastic materials," in *IEEE MTT-S Int. Microw. Symp. Digest, 2005.*, 2005, pp. 1409–1412.

[8] J. Hesselbarth, "Surface-mount cavity filter technology," in *2007 Eur. Microw. Conf.*, 2007, pp. 442–445.

[9] C. Lu, X. Yin, L. Xie, Q. Chen, and H. Zhao, "A miniaturized surface mount bandpass filter implemented with substrate integrated coaxial line," in *Proc. 2014 3rd Asia-Pacific Conf. Antennas Propag.*, 2014, pp. 1198–1200.

[10] J. Hesselbarth and R. Vahldieck, "Dual-mode surface-mount cavity resonator and filter," in *2009 IEEE MTT-S Int. Microw. Symp. Dig.*, 2009, pp. 1241–1244.

[11] M. D´ Auria, W. J. Otter, J. Hazell, B. T. W. Gillatt, C. Long-Collins, N. M. Ridler, and S. Lucyszyn, "3-D printed metal-pipe rectangular waveguides," *IEEE Trans. Compon., Packag. Manuf. Technol.*, vol. 5, no. 9, pp. 1339–1349, Sep. 2015.

[12] J. Rao, K. Nai, P. Vaitukaitis, Y. Li, and J. Hong, "3-D metal printed compact high-q folded waveguide filter with folded antenna," *IEEE Trans. Microw. Theory Techn.*, vol. 70, no. 1, pp. 112–121, 2022.

[13] Y. Chen, G. Zhang, J. Hong, Z. Sun, J. Yang, W. Tang, and C. Feng, "3-D printed dual-band filter based on spherical dual-mode cavity," *IEEE Microw. Wireless Compon. Lett.*, vol. 31, no. 9, pp. 1047–1050, 2021.

[14] H. Garca-Martínez, E. Avila-Navarro, G. Torregrosa-Penalva, N. Delmonte, L. Silvestri, S. Marconi, G. Alaimo, F. Auricchio, and M. Bozzi, "Design and fabrication of a band-pass filter with EBG single-ridge waveguide using additive manufacturing techniques," *IEEE Trans. Microw. Theory Techn.*, vol. 68, no. 10, pp. 4361–4368, 2020.

[15] B. Al-Juboori, J. Zhou, Y. Huang, M. Hussein, A. Alieldin, W. J. Otter, D. Klugmann, and S. Lucyszyn, "Lightweight and low-loss 3-d printed millimeter-wave bandpass filter based on gap-waveguide," *IEEE Access*, vol. 7, pp. 2624–2632, 2019.

[16] L. Zhu, R. Payapulli, S.-H. Shin, M. Stanley, N. M. Ridler, and S. Lucyszyn, "3-d printing quantization predistortion applied to sub-thz chained-function filters," *IEEE Access*, vol. 10, pp. 38 944–38 963, 2022.

[17] T.-Y. Huang, T.-M. Shen, and R.-B. Wu, "Design and modeling of microstrip line to substrate integrated waveguide transitions," in *Passive Microw. Compon. Antennas*, V. Zhurbenko, Ed. Rijeka: IntechOpen, 2010, ch. 11. [Online]. Available: https://doi.org/10.5772/9418

[18] D. Liu, H. Nakano, X. Qing, and T. Zwick, Eds., *Handbook of Antenna Technologies*, 1st ed., ser. Handbook of Antenna Technologies. Singapore, Singapore: Springer, Jun. 2016.

[19] X. Huang and K.-L. Wu, "A broadband u-slot coupled microstrip-to-waveguide transition," *IEEE Trans. Microw. Theory Techn.*, vol. 60, no. 5, pp. 1210–1217, 2012.

[20] A. Belenguer, H. Esteban, and V. E. Boria, "Novel empty substrate integrated waveguide for high-performance microwave integrated circuits," *IEEE Trans. Microw. Theory Techn.*, vol. 62, no. 4, pp. 832–839, 2014.

[21] ——, "Novel empty substrate integrated waveguide for high-performance microwave integrated circuits," *IEEE Trans. Microw. Theory Techn.*, vol. 62, no. 4, pp. 832–839, 2014.

[22] R. J. Cameron, C. M. Kudsia, and R. R. Mansour, *Microwave Filters For Communication Systems : Fundamentals, Design and Applications*. Hoboken, NJ, USA: Wiley, 2018.

[23] R. J. Cameron, "Adv. filter synthesis," *IEEE Microw. Mag.*, vol. 12, no. 6, pp. 42–61, 2011.

[24] Federal Communications Commission, "5 GHz unlicensed spectrum (UNII)," Federal Communications Commission, Washington, D.C., Tech. Rep. 78 FR 21320, Oct. 2013. [Online]. Available: https://www.fcc.gov/document/5-ghz-unlicensed-spectrum-unii

[25] "High resolution SLA and SLS 3D printers for professionals." [Online]. Available: https://formlabs.com/

[26] D. Karalekas and A. Aggelopoulos, "Study of shrinkage strains in a stereolithography cured acrylic photopolymer resin," *J. Mater. Process. Technol.*, vol. 136, no. 1, pp. 146–150, 2003. [Online]. Available: https://www.sciencedirect.com/science/article/pii/S0924013603000281

[27] M. Dewaele, D. Truffier-Boutry, J. Devaux, and G. Leloup, "Volume contraction in photocured dental resins: The shrinkage-conversion relationship revisited," *Dental Mat.*, vol. 22, no. 4, pp. 359–365, 2006. [Online]. Available: https://www.sciencedirect.com/science/article/pii/S0109564105001855

[28] N. Zhu, Y. Hou, W. Yang, C. Zhong, L. Zhang, D. Wang, R. Zhang, L. Li, and G. Wen, "Additive manufacturing low shrinkage si-based composite ceramics with sico microsphere/polyvinyl silicon acetylene slurry," *J. Eur. Ceram. Soc.*, vol. 42, no. 15, pp. 6925–6934, 2022. [Online]. Available: https://www.sciencedirect.com/science/article/pii/S0955221922006318

[29] A. Tamayo-Dominguez, J.-M. Fernandez-Gonzalez, and M. Sierra-Perez, "Metal-coated 3D-Printed waveguide devices for mm-wave applications [application notes]," *IEEE Microw. Mag.*, vol. 20, no. 9, pp. 18–31, 2019.

[30] Q. Zhang, S. Weng, C. M. Hamel, S. M. Montgomery, J. Wu, X. Kuang, K. Zhou, and H. J. Qi, "Design for the reduction of volume shrinkage-induced distortion in digital light processing 3D printing," *Extreme Mech. Lett.*, vol. 48, p. 101403, 2021. [Online]. Available: https://www.sciencedirect.com/science/article/pii/S235243162100136X

[31] M. G. Eberhardt, A. M. Hodge, and P. S. Branicio, "Atomistic modeling of physical vapor deposition on complex topology substrates," *Comput. Mater. Sci.*, vol. 203, p. 111111, 2022. [Online]. Available: https://www.sciencedirect.com/science/article/pii/S0927025621007795

[32] H. A. Jehn, "PVD and ECD-competition, alternative or combination?" *Surf. Coatings Technol.*, vol. 112, no. 1, pp. 210–216, 1999. [Online]. Available: https://www.sciencedirect.com/science/article/pii/S0257897298007506

[33] K. Moraczewski, R. Malinowski, P. Rytlewski, and M. Zenkiewicz, "Autocatalytic metallization of polylactide," *Polimery*, vol. 60, no. 07/08, pp. 492–500, Jul. 2015.

[34] G. Mallory, *Electroless Plating: Fundamentals and Applications*. Orlando, Fla: The Society, 1990.

[35] LPKF. [Online]. Available: https://www.lpkf.com/en/industries-technologies/research-in-house-pcb-prototyping/pcb-prototyping-process-steps/through-hole-plating-solutions

[36] C. Guo, X. Shang, J. Li, F. Zhang, M. J. Lancaster, and J. Xu, "A lightweight 3-D printed X-band bandpass filter based on spherical dual-mode resonators," *IEEE Microw. Wireless Compon. Lett.*, vol. 26, no. 8, pp. 568–570, 2016.

[37] L. Qian, Y. Wang, S. Li, A. E.-M. A. Mohamed, M. M. Attallah, T. Skaik, P. Booth, L. Pambaguian, C. M. Espaa, and P. Martn-Iglesias, "A narrowband 3-D printed invar spherical dual-mode filter with high thermal stability for OMUXs," *IEEE Trans. Microw. Theory Techn.*, vol. 70, no. 4, pp. 2165–2173, 2022.

[38] X. Wen, C. Guo, X. Shang, Y. Yu, M. Shu, Q. Yang, S. Li, M. M. Attallah, H. Liu, and A. Zhang, "SLM printed waveguide dual-mode filters with reduced sensitivity to fabrication imperfections," *IEEE Microw. Wireless Compon. Lett.*, vol. 31, no. 11, pp. 1195–1198, 2021.

[39] C. Guo, X. Shang, M. J. Lancaster, and J. Xu, "A 3-D printed lightweight X-band waveguide filter based on spherical resonators," *IEEE Microw. Wireless Compon. Lett.*, vol. 25, no. 7, pp. 442–444, 2015.

[40] S. Sirci, E. Menargues, and S. Berry, "Triangular combline filters conceived for additive manufacturing," in *2021 IEEE MTT-S Int. Microw. Filter Workshop (IMFW)*, 2021, pp. 151–154.

[41] A. Perigaud, O. Tantot, N. Delhote, S. Bila, S. Verdeyme, and D. Baillargeat, "Continuously tunable filter made by additive manufacturing using a 3D spiral ribbon," in *2017 IEEE MTT-S International Microwave Workshop Series on Advanced Materials and Processes for RF and THz Applications (IMWS-AMP)*, 2017, pp. 1–3.

[42] H. García-Martínez, G. Torregrosa-Penalva, E. Ávila-Navarro, N. Delmonte, L. Silvestri, and M. Bozzi, "3D-printed electromagnetic band-gap band-pass filter based on empty single-ridge waveguide," *IEEE Access*, vol. 10, pp. 53 954–53 962, 2022.

[43] C. Mximo-Gutirrez, J. Hinojosa, and A. lvarez melcon, "Narrowband and wideband bandpass filters based on empty substrate integrated waveguide loaded with dielectric elements," *IEEE Access*, vol. 9, pp. 32 094–32 105, 2021.

[44] F. Zhu, Y. Wu, P. Chu, G. Q. Luo, and K. Wu, "Single-layer substrate-integrated waveguide inline filters with flexible transmission zeros,"

IEEE Microw. Wireless Compon. Lett., vol. 32, no. 6, pp. 495–498, 2022.

[45] F. Cheng, X. Q. Lin, M. Lancaster, K. Song, and Y. Fan, "A dual-mode substrate integrated waveguide filter with controllable transmission zeros," *IEEE Microw. Wireless Compon. Lett.*, vol. 25, no. 9, pp. 576–578, 2015.

[46] A. Basti, S. Bila, S. Verdeyme, A. Perigaud, L. Estagerie, and H. Leblond, "Design of a compact hybrid filter using microstrip resonators and surface mounted cavities," in *2014 IEEE MTT-S Int. Microw. Symp. (IMS2014)*, 2014, pp. 1–4.

[47] P. Chu, J. Feng, L. Guo, L. Zhang, L. Liu, and K. Wu, "Multilayer substrate integrated waveguide filter with multimode suppression and wide stopband," *IEEE Trans. Circuits Syst. II: Exp. Briefs*, vol. 69, no. 11, pp. 4553–4557, 2022.

[48] J. D. Martínez, S. Sirci, and V. E. Boria, "Compact SIW filter with asymmetric frequency response for C-band wireless applications," in *2013 IEEE Inter. Wireless Symp. (IWS)*, 2013, pp. 1–4.

[49] Formlabs, "Form 3 Dimensional Accuracy Report," Formlabs, Tech. Rep., May 2021. [Online]. Available: https://media.formlabs.com/m/31d467c9bde28d36/original/-ENUS-Form-3-Dimensional-Accuracy-Report.pdf

[50] S. Johann, F. William, P. Aurlien, T. Olivier, D. Nicolas, S. Bila, V. Serge, P. Jean-Baptiste, and R.-P. Gramond, "Plastic and metal additive manufacturing technologies for hyperfrequency passive components up to ka band," in *2016 46th Eur. Microw. Conf. (EuMC)*, 2016, pp. 373–376.

[51] M. Dionigi, C. Tomassoni, G. Venanzoni, and R. Sorrentino, "Simple high-performance metal-plating procedure for stereolithographically 3-D-printed waveguide components," *IEEE Microw. Wireless Compon. Lett.*, vol. 27, no. 11, pp. 953–955, 2017.

[52] E. A. Rojas-Nastrucci, J. T. Nussbaum, N. B. Crane, and T. M. Weller, "Ka-band characterization of binder jetting for 3-D printing of metallic rectangular waveguide circuits and antennas," *IEEE Trans. Microw. Theory Techn.*, vol. 65, no. 9, pp. 3099–3108, 2017.

Vicente Nova received the MSc in telecommunications engineering and the MSc in telecommunication technologies, systems and networks from the Universidad Politécnica de Valencia in 2016 and 2018 respectively. Since 2018, he has been with the institute of telecommunications and multimedia applications (iTEAM) of the Universitat Politécnica de Valéncia where he is currently pursuing the Ph.D degree. His current research interests include the design and manufacturing of substrate integrated microwave devices, the design of reconfigurable devices based on liquid crystals, and the application of additive manufacturing and metalization techniques for developing passive waveguide devices.

Carmen Bachiller received her MSc degree in Telecommunication Engineering in 1996 and her PhD in Telecommunication in 2010 from the Universidad Politécnica de Valencia (UPV). She worked from 1997 to 2001 in the ETRA I+D company as a project engineer in research and development on automatic traffic control, public transport management and public information systems using telecommunication technology. In 2001 she joined the Communication Department of the UPV as an assistant lecturer, she is an Associated Professor since 2011. She is teaching electromagnetism theory. She has participated in several research projects, teaching innovation projects and technological heritage studies. Her current research activities include modal methods for electromagnetic analysis, optimization and design of passive microwave structures, analysis and design of substrate integrated transmission lines and circuits, power effects in passive waveguide systems, liquid crystal reconfiguration in microwave passive devices and 3D manufacturing. She is co-author of more than 30 research articles and one patent. She is currently the curator of the Telecommunications Museum of UPV.

Jordi Pascual-Folch received his BSc degree in Telecommunication Technologies and Services Engineering in 2021 from the Universitat Politécnica de Valéncia (UPV). Currently, he is studying the MSc in Telecommunication Engineering and the MSc in Electronic Systems Engineering, both at the UPV. He has worked on the design and fabrication of microwave devices based on 3D printing in the Microwave Applications Group (GAM), belonging to the Institute of Telecommunications and Multimedia Applications (iTEAM) - UPV. He has also fully developed a web interface to display real-time information from drones, BUBBLES project, in the Institute of Information and Communication Technologies (ITACA) - UPV. Currently, he is working at MaxLinear, focusing mainly on wireless backhaul systems. His current research interests include the design, manufacturing, and analysis of passive microwave devices; and signal processing and algorithms design in wireless communications.

Álvaro Ferrer received the BSc degree in Telecommunication Technologies and Services Engineering in 2020 from the Universidad Politécnica de Valencia (UPV). Since 2021, he has been with the institute of telecommunications and multimedia applications (ITEAM) of the Universitat Politécnica de Valéncia where he is currently senior research technician in the Microwave Applications Group (GAM). His current research interests include design and implementation of microwave devices using 3D manufacturing and metalization techniques.

Luis N. Ponce-Gonzalez received a BSc in Chemistry from Universitat de València in 2020. During his undergraduate studies, he enjoyed a scholarship at Imperial College London and did an internship at Universität für Bodenkultur Wien. Following, he obtained a MSc in Green Chemistry at Instituto de Tecnología Química of Universitat Politècnica de València (ITQ, UPV-CSIC) in 2021, where he is currently pursuing a Ph.D degree in Sustainable Chemistry. His current research interests include the development and characterization of photocatalytic materials, the optimization of photoreactors for wastewater decontamination, and the metallisation of non-conductive polymeric substrates.

M. Luisa Marin was born in Valencia, Spain. She obtained her PhD in organic chemistry at the University of Valencia in 1995, working on the synthesis of natural products. She has spent postdoctoral periods at Imperial College (1996-1998, London, UK) and University of Ottawa (2006, 2012-2013, 2014, Ottawa, Canada). In 1998, she moved to the Technical University of Valencia (UPV) and started working in the field of photochemistry, photophysics and photobiology. Since 2001 she belongs to the Instituto de Tecnología Química (UPV-CSIC). In 2019, she was promoted to Full Professor at the Chemistry Department of the UPV. Dr. Marín has been awarded for the competition of the Distinguised Visiting Researcher Program at the University of Ottawa (2013-2014). Her current research interests are focussed on the synthesis, evaluation and mechanistic studies of heterogeneous photocatalysts for decontamination and disinfection of wastewaters. She is also currently involved in the development of conductive polymeric devices as well as in the minimization of the environmental impact of those processes.

Vicente E. Boria Esbert (Fellow, IEEE) was born in Valencia, Spain, in May 1970. He received the Ingeniero de Telecomunicación (Hons.) and Doctor Ingeniero de Telecomunicación degrees from the Universitat Politècnica de València, Valencia, Spain, in 1993 and 1997, respectively. In 1993, he joined the Departamento de Comunicaciones, UUniversitat Politècnica de València, where he has been Full Professor since 2003. In 1995 and 1996, he was holding a Spanish trainee position with the European Space Research and Technology Centre, European Space Agency (ESTEC-ESA), Noordwijk, The Netherlands, where he was involved in the area of EM analysis and design of passive waveguide devices. He has authored or coauthored ten chapters in technical textbooks, 180 papers in refereed international technical journals, and over 200 papers in international conference proceedings. His current research interests are focused on the analysis and automated design of passive components, left-handed and periodic structures, and the simulation and measurement of power effects in passive waveguide systems. Dr. Boria has been a member of the IEEE Microwave Theory and Techniques Society (IEEE MTT-S) and the IEEE Antennas and Propagation Society (IEEE AP-S) since 1992. He is also a member of the European Microwave Association (EuMA) and the Technical Committees of the IEEE-MTT International Microwave Symposium and the European Microwave Conference. He has been the Chair of the 48th European Microwave Conference held in Madrid, Spain. He acts as a regular reviewer of the most relevant IEEE and IET technical journals in his areas of interest. He was an Associate Editor of IEEE Microwave and Wireless Components Letters from 2013 to 2018 and Electronics Letters (IET) from 2015 to 2018. He also serves as a Subject Editor (Microwaves) for Electronics Letters (IET) and as an Editorial Board Member for International Journal of RF and Microwave Computer-Aided Engineering.